The S-Fe(Ni) sub-surface active sites for efficient and stable overall water splitting

Kun Feng [a,1], Ruru Song [a,1], Jiabin Xu [a], Yufeng Chen [a], Cheng Lu [a], Youyong Li [a,d], Werner Hofer [b], Haiping Lin [a,c,*], Zhenhui Kang [a,d,*], Jun Zhong [a,**]

[a] *Institute of Functional Nano and Soft Materials Laboratory (FUNSOM), Jiangsu Key Laboratory of Advanced Negative Carbon Technologies, Soochow University, Suzhou 215123, China*
[b] *University of Chinese Academy of Sciences, Beijing 100093, China*
[c] *School of Physics and Information Technology, Shaanxi Normal University, Xi'an 710062, China*
[d] *Macao Institute of Materials Science and Engineering (MIMSE), MUST-SUDA Joint Research Center for Advanced Functional Materials, Macau University of Science and Technology, Taipa 999078, Macao, China*

ABSTRACT

Balancing catalytic efficiency and stability is always a critical and challenge issue for energy related research. Here we propose a reaction reconstruction strategy to create active sites in the sub-layer of sulfur-modified transition metal-based catalysts, which can both achieve a high efficiency and exhibit an excellent stability for overall water splitting. The sub-layer active sites of S-Fe and S-Ni are evidenced by the bulk-sensitive X-ray absorption spectroscopy (XAS), while they cannot be observed by the surface-sensitive X-ray photoelectron spectroscopy. Theoretical calculations reveal that the sub-layer active sites can promote the water dissociation and accelerate the formation of high-energy peroxyl groups in anodes to achieve a high efficiency, while the surface layer can protect the sub-layer sites for excellent stability. The high stability is also confirmed by in-situ XAS. As a result, the obtained bi-functional catalyst as both cathode and anode can achieve a current density of 10 mA cm^{-2} for overall water splitting at a low cell voltage of 1.53 V (1.81 V for 100 mA cm^{-2}), with an excellent stability over 200 h, which outperforms the benchmark Pt/C-RuO$_2$/NF electrodes.

1. Introduction

With ever-increasing energy demand and the ensuing environmental crisis, extensive efforts have been made for the generation of sustainable and clean energy [1–3]. Among fossil-free energy resources, hydrogen energy is highly desirable due to zero CO$_2$ emission, high energy density and the green "electrochemical water cycle" [1,4,5]. The electrochemical water splitting to produce hydrogen consists of two half reactions: cathodic hydrogen evolution reaction (HER) and anodic oxygen evolution reaction (OER) [2,4,6]. Currently, Pt based and Ir/Ru based materials are the benchmark catalysts for HER and OER [7–9], respectively. However, noble metal-based catalysis is expensive. Moreover, the mismatched catalytic environments for HER and OER with different catalysts typically lead to poor performance and the bi-functional

catalysts for both HER and OER are highly required for overall water splitting [10–12]. As a result, only around 4% of the hydrogen production today is accomplished by water electrolysis. Developing efficient, stable, and low-cost bi-functional catalysts for both HER and OER is thus of great significance. Unfortunately, this task is always challenged by how to balance the catalytic efficiency and the long-term stability with non-noble elements in harsh reaction environments.

Transition metal-based materials are typically not expensive, which have been widely used for energy related research. However, the catalytic activities of pure transition metals or metal oxides are normally not good enough, which could be improved by various modifications. Sulfur-based treatments in transition metals or metal oxides have been widely reported to exhibit good catalytic activities, and some of the resulted catalysts are even superior to the benchmark catalysts in both

HER and OER [13–18]. For instance, Zheng et al. reported that Cu_2O, which was inefficient in both HER and OER, exhibited satisfactory activity in overall water splitting after S-treatment [19]. Yu et al. also showed that S-doped CoO could drive overall water splitting at 10 mA cm^{-2} with a low cell voltage of 1.63 V in an alkaline media [20]. Although S-treated catalysts showed high activities, unfortunately, they were typically not stable in harsh reaction environments, especially in the oxidative OER process [13,14,19–21]. The active metal-sulfur compounds that formed via S-treatment, would quickly decrease during catalysis or even disappear in alkaline OER [19]. Except for S-treated metal oxides, similar unstable phenomena had also been widely reported in metal sulfides such as FeS [22], CoS_x [23,24], MoS_2/NiS_2 [25, 26] and MoS_2 [14]. All these materials have the problem of oxidation induced desulfurization on surfaces in OER, leading to unstable S-based active sites.

Bearing these experimental results in mind, in the present work we propose a reaction restructuring strategy to create active metal-S sites in the sub-layer of FeNi-based layered double hydroxide (FeNi-LDH), which can both achieve a high efficiency and exhibit an excellent stability for overall water splitting. The active sites of metal sulfides such as Ni-S or Fe-S can be clearly observed in the catalysts before and after both OER or HER reactions by using bulk-sensitive X-ray absorption spectroscopy (XAS), but they cannot be observed from the surface-sensitive X-ray photoelectron spectroscopy (XPS) after OER. This indicates that the active metal sulfides in OER are actually located in the sub-layer of the catalyst, keeping the high catalytic activity while protected by the surface layer. Density functional theory (DFT) calculations show that the embedded metal sulfide sites can promote the water dissociation in HER and significantly accelerate the formation of high-energy peroxyl groups in OER, resulting in outstanding overall water splitting performance. Experimentally, the resulted S-FeNi/NF catalyst demonstrates excellent and stable water splitting activity in the alkaline electrolyte, with a current density of 10 mA cm^{-2} at small overpotentials of 220 mV and 85.5 mV (vs. RHE) for OER and HER, respectively. This also enables low cell voltages of 1.53 V and 1.81 V (vs. RHE) to achieve 10 and 100 mA cm^{-2} for overall water splitting with an excellent stability over 200 h, respectively, outperforming the benchmark Pt/C-RuO_2 electrodes (1.55 and 1.90 V).

2. Experimental section

2.1. Chemicals and reagents

Iron nitrate nonahydrate (Fe(NO_3)$_3$·9 H_2O, 99.0%), ammonium fluoride (NH_4F, 96.0%) and anhydrous ethanol were bought from Sinopharm Chemical Reagent Co., Ltd. Potassium hydroxide (KOH, 85.0%) and thioacetamide (TAA, 99%) were purchased from Shanghai Macklin Biochemical Co., Ltd. Commercial Pt/C (20 wt%), RuO_2 (99.9%), urea (CO(NH_2)$_2$, 99.0%) and Nafion® perfluorinated resin solution were purchased from Sigma-Aldrich. Nickel foam was purchased from Innochem Technology Co., Ltd. All the reagents were analytical grade and used as received without further purification. Deionized water was obtained from an ultra-pure purifier (resistivity ≥18.2 MΩ).

2.2. Synthesis of FeNi-LDH/NF

One piece of nickel foam (2 × 4 cm^2, cleaned by ultrasonication for ten minutes with acetone, ethanol, 5 wt% HCl and water, respectively) was immersed into a 70 ml water solution containing 0.0166 M Fe (NO_3)$_3$·9H_2O, 0.125 M NH_4F and 0.25 M urea in a Teflon-lined stainless steel autoclave and then heated at 120 °C for 6 h in an electric oven. Thus the product named FeNi-LDH/NF could be obtained.

2.3. Synthesis of S-FeNi/NF

The above product was placed into a Teflon autoclave containing 50 ml EtOH solution and 2 mmol TAA. Then the temperature was increased from room temperature to 120 °C, keeping for 6 h. The resulted product was washed with ethanol for several times, and then dried in vacuum for 6 h. Finally, the S-treated FeNi-LDH on NF (denoted as S-FeNi/NF in the paper) could be obtained.

2.4. Structural characterization

The samples were measured by high-resolution transmission electron microscope (HRTEM) (FEI Talos F200X) and Scanning Electron Microscope (SEM, FEI Quanta 200 F). The Fe and S contents were measured by an inductively coupled plasma (ICP) spectrometer (ICP-MS, Agilent 7700X). X-ray photoelectron spectrometer (XPS, Kratos AXIS UltraDLD) and X-ray diffraction (XRD, PANalytical B.V. Empyrean powder diffractometer equipped with PIXcel3D detector) were also used for the structure characterization. X-ray absorption spectroscopy experiments were performed at the National Synchrotron Radiation Laboratory (NSRL, Beamlines MCD-A and MCD-B (Soochow Beamline for Energy Materials)), Taiwan Synchrotron Radiation Research Center (NSRRC, 01 A, 17 C and 16 A), and Shanghai Synchrotron Radiation Facility (SSRF, 11B).

2.5. Electrochemical measurement

All electrochemical measurements were carried out in a standard three electrode cell system using a CHI-760E electrochemical workstation at room temperature (~25 °C), where an Hg/HgO electrode and a graphite rod served as the reference electrode and the counter electrode, respectively. S-FeNi/NF with a size of 0.5 cm × 0.5 cm was used as the working electrode. For the RuO_2 and 20 wt% Pt/C electrodes, the catalysts (4 mg) were firstly dispersed in 1 ml Nafion solution (5 wt%) mixing with EtOH and water, and then sonicated for 30 min to form a homogeneous ink. 125 μl of the solution was loaded onto the Ni foam through drop-coating. All tests were measured in 1.0 M KOH solution, and the potential was normalized to reversible hydrogen electrode (RHE) by: E (RHE) = E (Hg/HgO) + 0.098 + 0.059 *pH. For OER measurements, cyclic voltammetry (CV) curves have been tested from 1.0 V to 2.0 V vs. RHE at a scan rate of 2 mV s^{-1}. For HER measurements, linear sweep voltammetry (LSV) curves have been tested from 0.1 V to − 0.6 V vs. RHE at a scan rate of 2 mV s^{-1}. Electrochemical impedance spectroscopy (EIS) was carried out at applied current density of 10 mA cm^{-2} over a frequency range from 0.1 Hz to 100 kHz with an additional alternating voltage at 5 mV. The electrochemically active surface area (ECSA) was estimated from the double layer capacitance (C_{dl}) charging curve using cyclic voltammetry in a small potential range (1.1–1.2 V vs. RHE) and the scan rates were 10, 20, 40, 60, 80 and 100 mV s^{-1}, respectively. The stability measurement was evaluated using 5000 continuous cycles from − 0.15–0.1 V (vs. RHE) for HER and 1.3–1.55 V (vs. RHE) for OER, respectively, at a scan rate of 100 mV s^{-1}. The stability tests were performed using the constant potential electrolysis method. To reveal the structural evolution during catalysis, the S-FeNi/NF catalysts after several OER or HER polarization cycles, as labeled as A-S-FeNi/NF (Anode for OER) or C-S-FeNi/NF (Cathode for HER), are also probed for comparison.

2.6. DFT calculations

DFT computations were conducted with the Vienna Ab-initio Simulation Package (VASP) code [27,28]. The Perdew-Burke-Ernzerhof (PBE) approximation of generalized gradient approximation (GGA) is employed to treat the exchange correlation energy and a kinetic energy cut-off of 450 eV is used for plane-wave propagation [29]. The DFT-D3 method with Becke-Jonson damping was used to correct the Van der

Waals interactions between OER intermediates and the catalyst. The catalyst is mimicked with a NiO_2 layer, with a Ni atom replaced by a Fe atom and two O atoms replaced by S atoms. A vacuum space of 25 Å is adopted to avoid neighboring image interactions along the z-direction and a $4 \times 4 \times 1$ Monkhorst-Pack k-point mesh was used to sample the Brillouin zone for structural and energy calculations. The Gibbs free energy change (ΔG) of each elemental step was calculated according to the following equation: $\Delta G = \Delta E + \Delta ZPE - T\Delta S + \Delta G_{pH}$, where E is the total energy directly obtained from DFT calculations, ZPE is the zero-point energies, T is the temperature (T = 298.15 K), and S is the entropy. The OER calculations consist of elementary steps including catalytic splitting of water molecules over metal atoms, the adsorption and co-adsorption of hydroxyl groups (*OH) on Fe, Ni and S atoms, the dehydrogenation of *OH to produce *O, the conversion of *O to *OOH, and the formation of *OOH at Fe, Ni and S atoms.

3. Results and discussion

3.1. Morphology and structure characterization

The catalysts were prepared through a two-step hydrothermal treatment. The synthetic process has been illustrated in the Experimental Section. Briefly, FeNi-LDH has been synthesized on Nickel foam (NF) (labeled as FeNi-LDH/NF) and then reacted with thioacetamide to obtain the S-treated sample (S-FeNi/NF). Then the samples have been used in OER (A-S-FeNi/NF) and HER (C-S-FeNi/NF) for several circles to finally form the real catalysts for overall water splitting [24,30]. The samples have been illustrated in Fig. 1a. X-ray diffraction (XRD) data of the samples are shown in Fig. S1, in which the major sharp peaks at about 45 and 52 degrees can be attributed to Ni foam. For FeNi-LDH/NF, the diffraction peaks around 12, 24, 35, 40, 47 and 60 degrees can be assigned to the characteristic peaks of FeNi-LDH [31,32]. However, the crystal peaks except for those of Ni foam are very weak in the S-treated sample, suggesting a possible amorphous structure of S-FeNi/NF with the harsh reaction in autoclave. The XRD patterns of S-FeNi/NF catalysts after several OER or HER cycles are also shown in Fig. S1b, without obvious crystalline peaks. The corresponding scanning electron microscope (SEM) images of FeNi-LDH/NF, S-FeNi/NF, and A-S-FeNi/NF are shown in Fig. 1(b-d) (Fig. S2 shows the large scale images). For FeNi-LDH/NF, some nanosheets stacked as microflowers are observed on NF. The clear nanosheet structure becomes thicker and disorganized after S-treatment, in agreement with the XRD data for the destroyed crystal structure. For A-S-FeNi/NF, the microstructures exhibit sphere-like morphologies due to the OER reaction. Transmission electron microscope (TEM) images and dark field energy dispersive X-ray spectroscopy (EDX) elemental mappings for FeNi-LDH/NF, S-FeNi/NF, A-S-FeNi/NF and C-S-FeNi/NF are shown in Figs. S3, 1(e, f), 1(g, h) and S4, respectively. The Fe, Ni and O elements are uniformly distributed in all the samples. Strong S signal can be clearly observed in S-FeNi/NF (Fig. 1f), suggesting the successful S-treatment. However, after OER and HER, the A-S-FeNi/NF and C-S-FeNi/NF samples (Figs. 1h and S4) show much weaker S signal, suggesting the loss of S during reaction.

X-ray photoelectron spectroscopy spectra of the three samples are shown in Fig. 2. Fig. 2a exhibits the survey scans while Fig. 2(b-d) are the high-resolution spectra. For FeNi-LDH/NF, the Ni 2p spectrum shows a main Ni $2p_{3/2}$ peak at 855.7 eV for Ni^{2+} (Fig. 2c), while the Fe 2p spectrum in Fig. 2b shows a position for Fe^{3+} (712.3 eV for Fe $2p_{3/2}$ and 725 eV for Fe $2p_{1/2}$), consistent with the typical LDH structure [32–34]. The major Ni^{2+} and Fe^{3+} peaks can also be observed in S-FeNi/NF in Fig. 2c and b, respectively. However, the existence of Fe-S species is indicated by a small new peak appearing at 707.0 eV in the Fe 2p XPS spectrum [35,36]. The new peak at 852.9 eV in Ni 2p XPS spectrum can also be observed for the presence of Ni-S species [17,18,37]. The formation of metal sulfides is also confirmed by peaks at 162.1 eV ($2p_{3/2}$) and 163.5 eV ($2p_{1/2}$) in S 2p XPS spectrum of S-FeNi/NF (Fig. 2d). Another S peak located at around 168.5 eV can be assigned to SO_4^{2-} due

to the oxidized S species [38,39]. The results suggest a successful S-treatment in S-FeNi/NF to create the active metal-S sites for efficient water splitting. However, after OER reaction, all the featured peaks of metal-S sites in A-S-FeNi/NF disappear in Fe, Ni, and S 2p XPS spectra (Fig. 2b–d), except for the residue signal of oxidized SO_4^{2-} in Fig. 2d, suggesting the significant loss of S after OER. The removal of S in A-S-FeNi/NF can also be observed in the survey scan in Fig. 2a. The K signal in A-S-FeNi/NF comes from the OER solution. The loss of S after OER is consistent with those reported in the literature [14,19,22,25]. In the highly oxidative OER environment, metal sulfides could be oxidized to form sulfate, which might be dissolved in the reaction solution resulting in the loss of S. The observed SO_4^{2-} in the catalyst may also partly come from the solution residue. Interestingly, the present S-treated sample after OER can still maintain its high performance for a long time, as illustrated in the catalytic part. Thus the true active sites in the catalysts should be carefully studied. The sample after HER reaction (C-S-FeNi/NF) also exhibits decreased amount of S as shown in Fig. S5. However, both sulfate and metal sulfides can still be observed in Fig. S5c, suggesting that in the reductive HER environment the active metal sulfides can be partly left for the reaction. Thus in this work the critical role of S has been mainly studied in the OER process.

3.2. Synchrotron radiation study

The catalysts have been further investigated by using X-ray absorption spectroscopy. As stated above, the XPS analysis indicates the formation of Fe-S and Ni-S bonds in the S-FeNi/NF catalyst. However, these featured peaks disappear after OER reaction. Actually, XPS is only a surface-sensitive method and the internal components under the surface layer of the catalysts may not be detected by XPS. To fully understand the compositions in the catalysts, a complete structural characterization including both bulk and surface information is highly required. Thus synchrotron radiation based XAS is selected to further identify the chemical status of sulfur in A-S-FeNi/NF and C-S-FeNi/NF, because of its high chemical sensitivity and tunable detection depth. XAS can detect both surface and bulk information (more than 1 μm) by selecting different detection modes or different energy ranges. For example, XAS in the hard or tender X-ray range with fluorescence mode or transmission mode is typically bulk-sensitive while XAS in soft X-ray range with electron yield mode is more surface-sensitive (a few nm). Since XPS mainly probes the surface signal (1–2 nm), we have measured the Fe, Ni and S K-edge XAS spectra with deeper structure information to probe the S effect in A-S-FeNi/NF and C-S-FeNi/NF. The detection capabilities for XPS and XAS (hard and tender X-ray range) are also illustrated in Fig. 3a.

Fig. 3b shows the normalized X-ray Absorption Near Edge Structure (XANES) spectra of samples at the Fe K-edge. The XANES spectrum of FeNi-LDH/NF shows a pre-edge peak A1 at around 7115 eV and a strong white line peak A2 at around 7133 eV, which is very similar to that of the Fe_2O_3 reference for Fe^{3+}. The corresponding Extended X-ray Absorption Fine Structure (EXAFS) data in Fig. 3c also shows a strong peak for the Fe-O bond [40], confirming the Fe^{3+} chemical state in FeNi-LDH/NF. Interestingly, after S-treatment the S-FeNi/NF sample shows a red shift of the white line peak in Fig. 3b, suggesting a reduced oxidation state of Fe. This spectral change can be attributed to the formation of a Fe-S bond [41], as compared with the reference FeS_2 sample (Fig. S6a). The EXAFS data of S-FeNi/NF in Fig. 3c also shows a new peak revealing the existence of a Fe-S bond [42,43], which is similar to that of the reference FeS_2 sample (Fig. S6b). However, the Fe-S peak intensity for A-S-FeNi/NF after several OER cycles sharply decreases in Fig. 3c, indicating the loss of S. More evidence for the loss of S can be found in the wavelet transform (WT) plots in Fig. S6c, which can display both k-space and R-space data in a 2D way to discriminate the backscattering atoms [44]. The XAS spectra of C-S-FeNi/NF also show similar results (Fig. S7).

To carefully analyze the EXAFS data, the curves have been fitted as shown in Fig. S8 and Table S1. Compared with the fresh-prepared S-
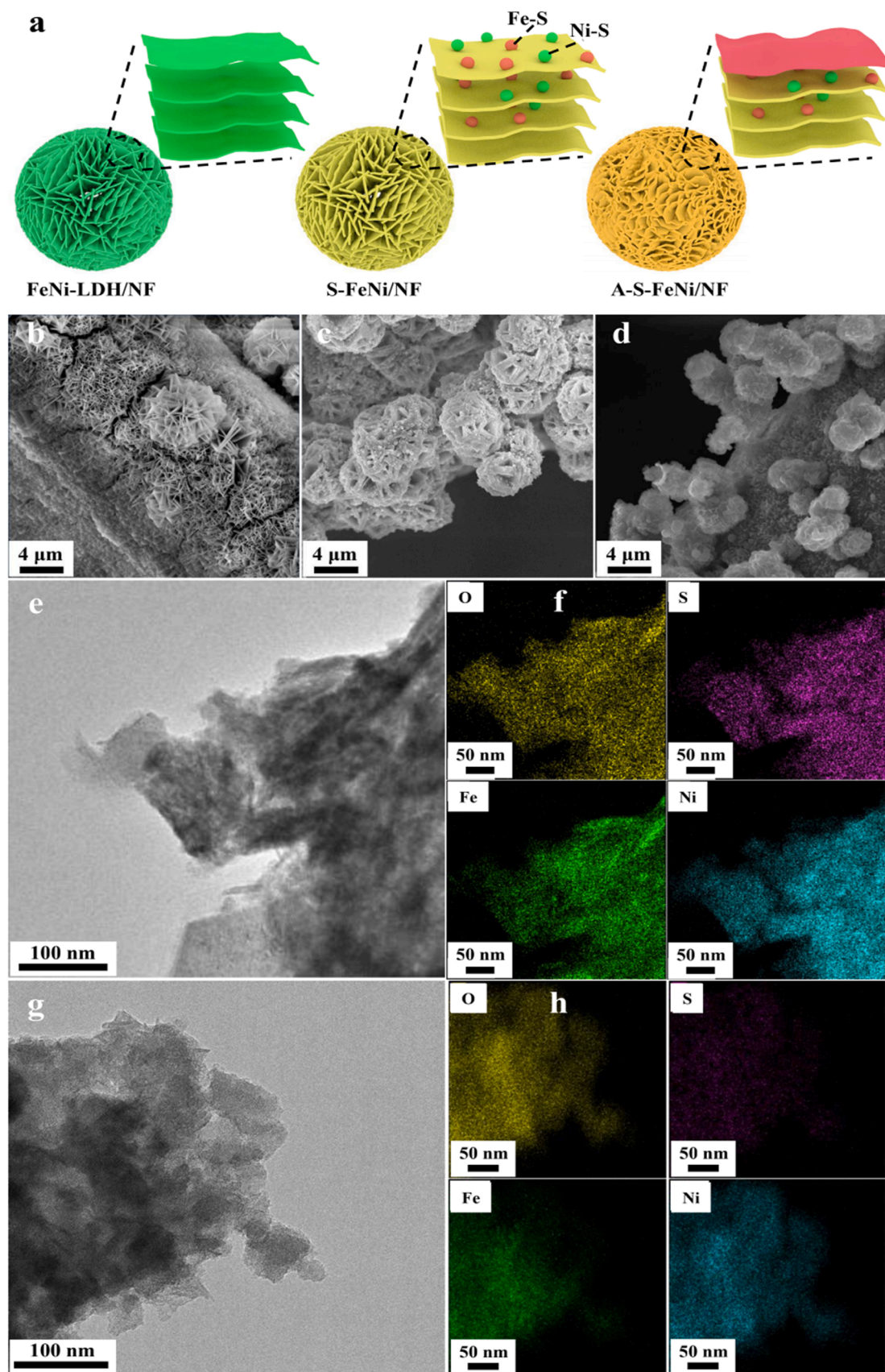
Fig. 1. Morphology information of S-treated FeNi/NF. (a) Schematic illustration for the preparation of various catalysts. SEM images of (b) FeNi-LDH/NF, (c) S-FeNi/ NF and (d) A-S-FeNi/NF. (e) TEM image and (f) dark field elemental mappings of S-FeNi/NF. (g) TEM image and (h) dark field elemental mappings of A-S-FeNi/NF. Mapping colors: O (yellow), S (purple), Fe (green) and Ni (blue).
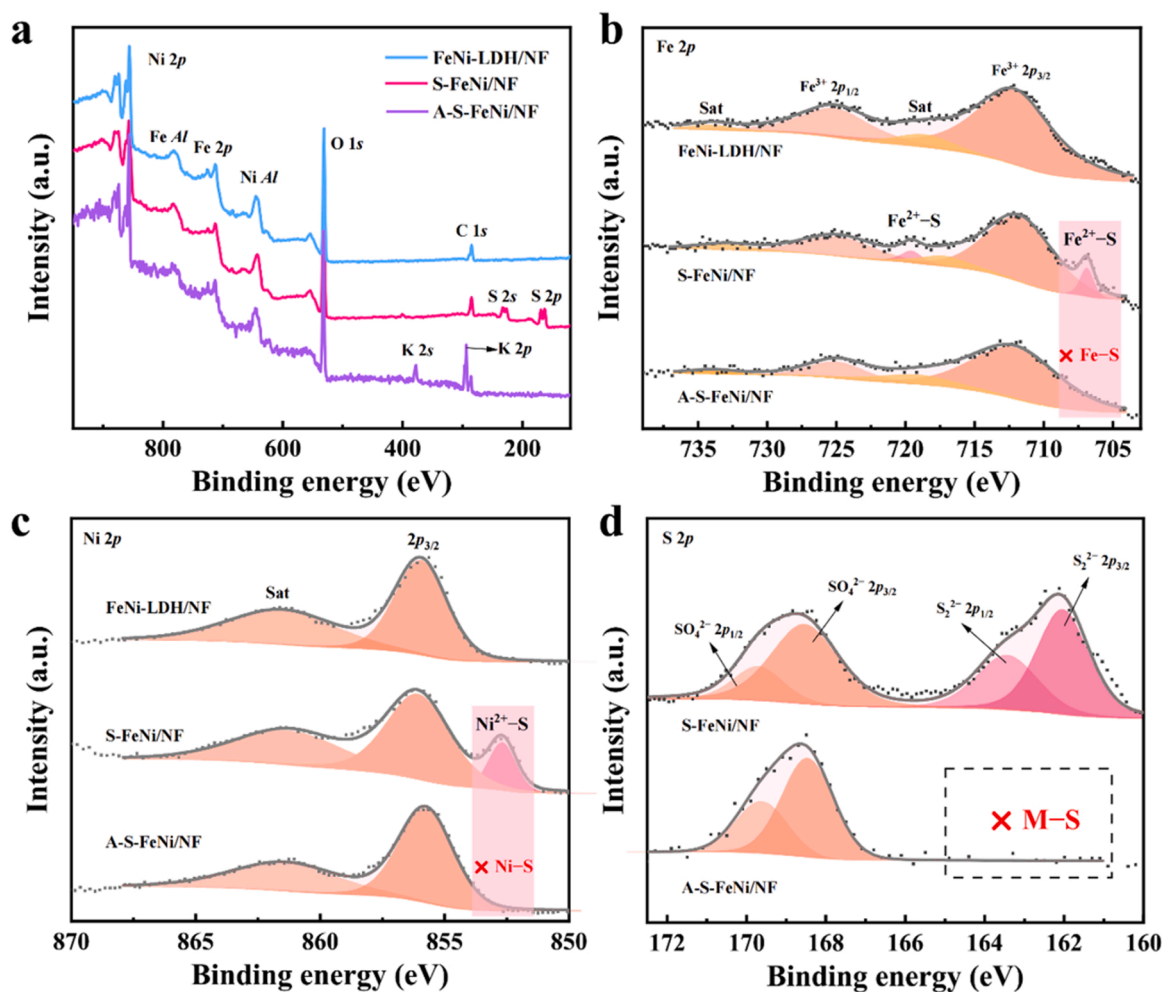
Fig. 2. XPS spectra of the samples. XPS survey scans (a), Fe *2p* (b) and Ni *2p3/2* (c) spectra of FeNi-LDH/NF, S-FeNi/NF and A-S-FeNi/NF, respectively. (d) S *2p* spectra of S-FeNi/NF and A-S-FeNi/NF.

FeNi/NF, the coordination number (CN) of Fe-O and Fe-S are significantly changed after several OER or HER cycles. The CN_{Fe-O} of A-S-FeNi/NF increases from 1.93 (before OER reaction) to 4.54 (after OER reaction), while CN_{Fe-S} reduces dramatically from 1.67 to 0.17. The C-S-FeNi/NF sample shows similar changes. The results reveal the significant decrease of Fe-S bonds after OER and HER reactions in the samples. However, there are still some weak signals for Fe-S according to the fitting (CN=0.17), suggesting the partial existence of a Fe-S composite. The existence of Fe-S features can also be observed in the WT plots in Figs. S6c and S7c. XAS detects the average signal of an element. Due to the large amounts of Fe-O based composites in the catalyst after OER, the detected Fe-S signal can be weak but the fitting results clearly confirm its existence. The XANES and EXAFS spectra at Ni *K*-edge are also shown in Fig. S9. Unfortunately, XAS at Ni *K*-edge is bulk-sensitive and the Ni signals in catalysts have been significantly submerged by those of Ni substrate [45].

In order to further understand the compositions of catalyst, the S *K*-edge XAS spectra are also measured with a fluorescence mode (Fig. 3d and e). S *K*-edge XAS is one of the most direct methods to probe the S-based materials since it will not be affected by the bulk Fe or Ni. After S-treatment, the S signals of iron disulfide (Fe-S bond) and nickel disulfide (Ni-S bond) can be clearly identified by comparing with reference samples. The featured peak at around 2482 eV can be assigned to a S-O bond similar to that in SO_4^{2-} [46], in good agreement with the XPS results for oxidized sulfur. After OER and HER reactions (A-S-FeNi/NF and C-S-FeNi/NF), the intensities for Fe-S and Ni-S peaks at 2471 and

2472 eV also decrease. However, these peaks are still clear and strong in both A-S-FeNi/NF and C-S-FeNi/NF, even after 5000 catalytic cycles, significantly different from the surface-sensitive XPS results. This important phenomenon strongly confirms the existence of Fe-S and Ni-S as active species in A-S-FeNi/NF and C-S-FeNi/NF, even after long-term electrocatalysis. Since S *K*-edge XAS with fluorescence mode has a deeper detection depth than that of surface-sensitive XPS, the Fe-S and Ni-S species are actually located in the near surface (sub-layer) or bulk regions of the catalysts which are hard to be detected by XPS. Therefore, a suitable XAS measurement at the S *K*-edge could be used to accurately reveal the existence of Fe-S and Ni-S species (such as FeS_2 and NiS_2) when the reaction restructuring occurs, which might be the sub-layer active sites responsible for the efficient electrocatalytic reactions.

3.3. Electrocatalytic activity

The electrocatalytic activities of FeNi-LDH/NF and S-FeNi/NF in OER and HER were evaluated using a standard three-electrode cell in 1.0 M N_2-saturated KOH. The catalysts on NF were cut into 0.5 * 0.5 cm and used as the working electrode. The measurements were performed at 2 mV s^{-1} after 85% *iR* compensation at 25 °C. Details of measurements can be found in the experimental part. The Fe and S contents measured by ICP are shown in Table S2. Since the initial S-FeNi/NF catalyst will change its structure during the reaction (Figs. 2 and 3), the stable samples after several OER (A-S-FeNi/NF) or HER (C-S-FeNi/NF) cycles are used for the performance comparison in Fig. 4 (S-FeNi/NF
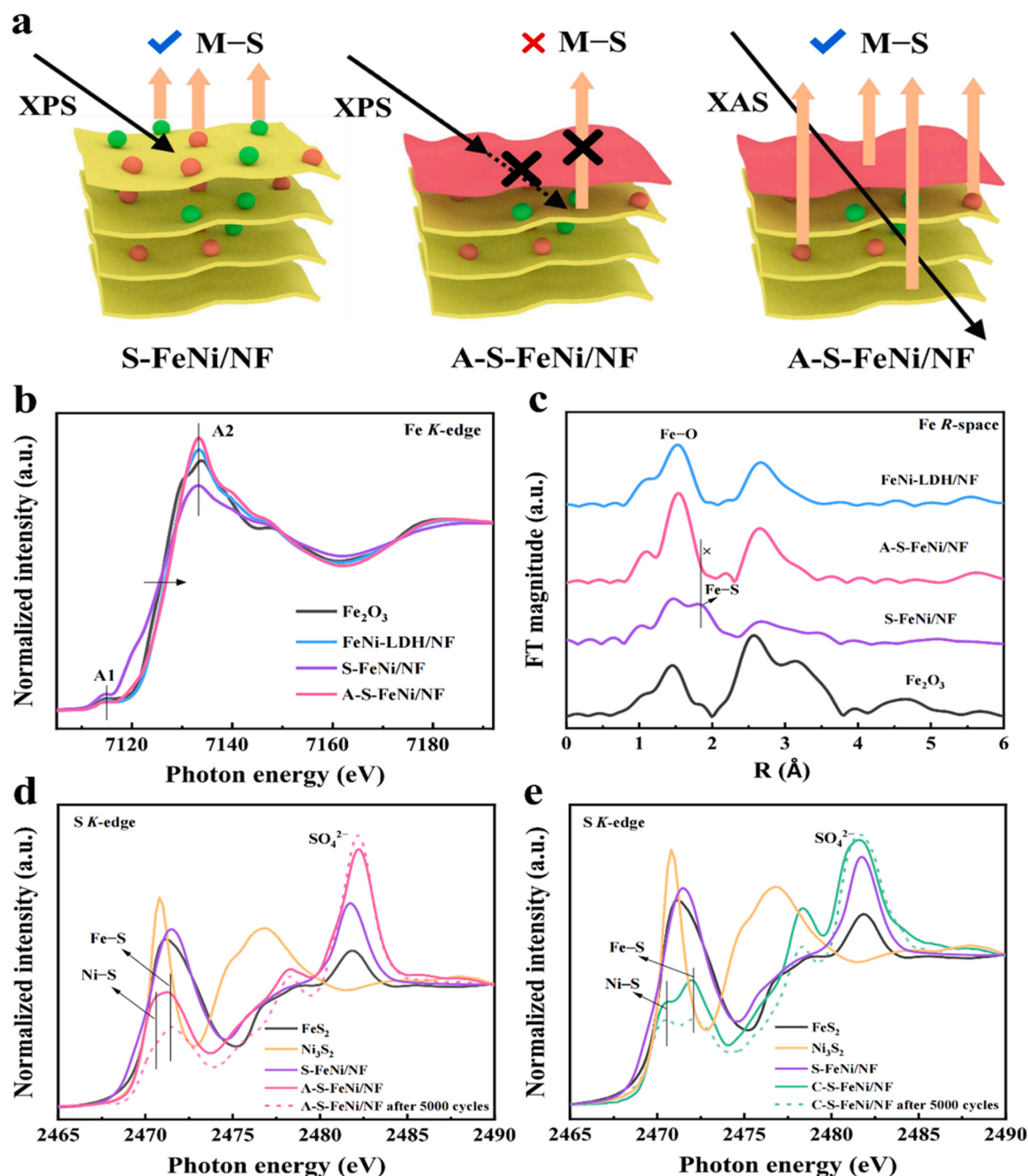
Fig. 3. Fe and S K-edge XAS spectra of various catalysts. (a) Illustration for the detection depth of XPS and XAS. (b) XANES spectra of Fe₂O₃, FeNi-LDH/NF, S-FeNi/NF and A-S-FeNi/NF at Fe K-edge, respectively. (c) Fourier transform curves of the EXAFS data at Fe K-edge. (d) S K-edge XAS spectra of S-FeNi/NF, A-S-FeNi/NF and that after 5000 CV cycles (OER). (e) S K-edge XAS spectra of S-FeNi/NF, C-S-FeNi/NF and that after 5000 CV cycles (HER). The reference spectra of FeS₂ and Ni₃S₂ are also shown for comparison.

shows almost the same electrocatalytic performance to that of A-S-FeNi/NF and C-S-FeNi/NF).

The electrocatalytic OER curves of NF, FeNi-LDH/NF, A-S-FeNi/NF and RuO₂ electrocatalysts are shown in Fig. 4a. The strong peaks around 1.4 V are attributed to the oxidation of Ni^{2+} to Ni^{3+}. Therefore, the latter half of the CV curve without the influence of oxidation peaks is selected to calculate OER activity [40,47]. As shown in Figs. 4a and S10, the NF exhibits poor activity in OER, which only serves as the substrate in catalysis. RuO₂/NF has been employed as the benchmark catalyst to evaluate the performance of FeNi-LDH/NF and A-S-FeNi/NF. As seen in Fig. 4a, RuO₂/NF shows a good OER activity with a small overpotential of 296 mV at a current density of 10 mA cm⁻², which is in good

agreement with previous experimental results [40]. Comparing with RuO₂/NF, FeNi-LDH/NF exhibits a higher catalytic activity by driving OER at a smaller overpotential (245 mV) at the same current density. After S-treatment, remarkably, the OER on A-S-FeNi/NF has been further improved, resulting in a low overpotential of 220 mV at a current density of 10 mA cm⁻². The energy conversion efficiency of OER on A-S-FeNi/NF is therefore 25.7% higher than that on RuO₂/NF. For comparison, the onset overpotentials and the overpotentials at 10 mA cm⁻² for all samples are also shown in Fig. S10, in which A-S-FeNi/NF shows the lowest values. The enhanced catalytic activity of A-S-FeNi/NF is also consistent with its lowest Tafel slope of 36.6 mV dec⁻¹ in Fig. 4c, as compared with those of pure NF (100.3 mV dec⁻¹),
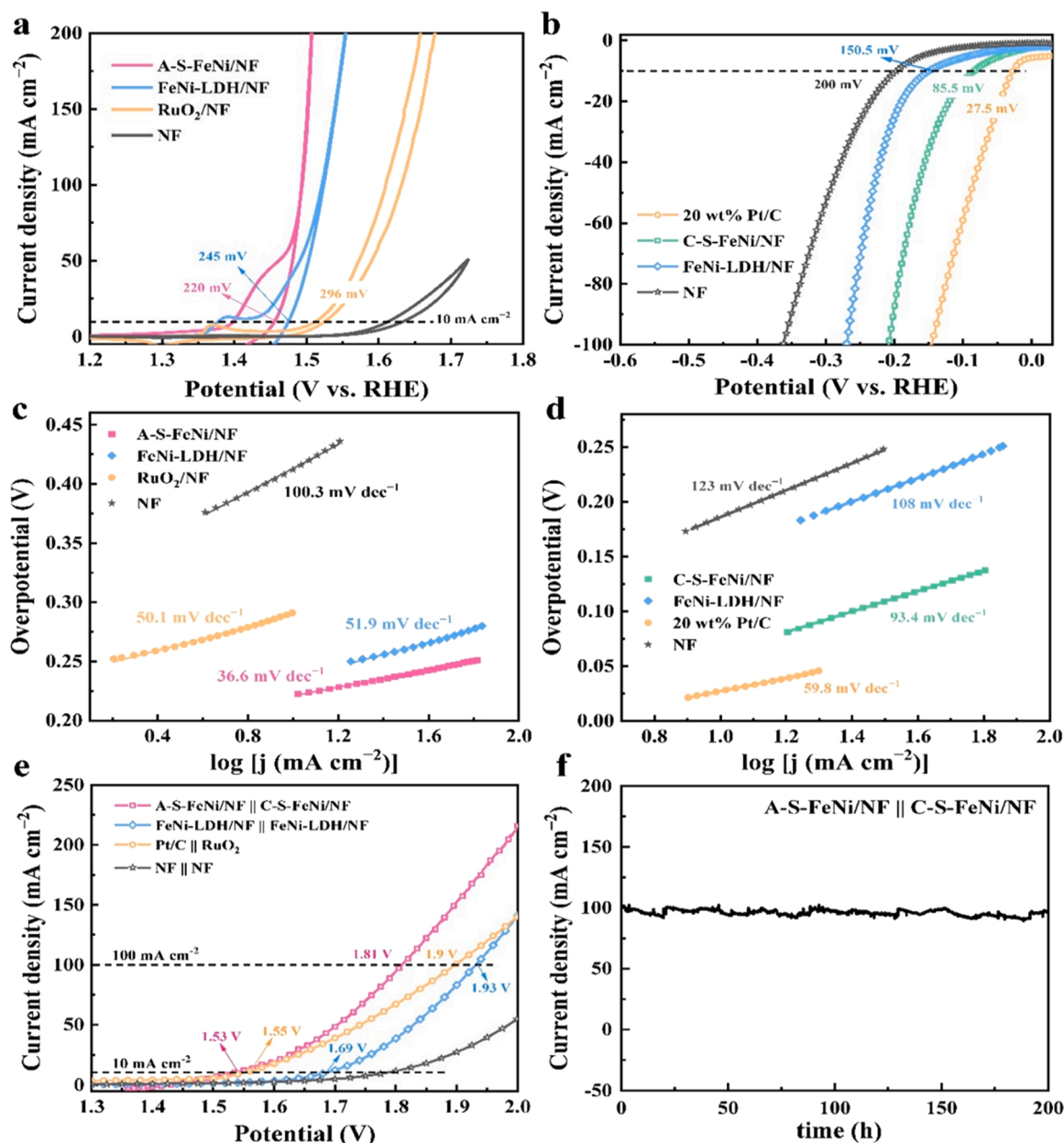
Fig. 4. Electrochemical properties of the catalysts for overall water splitting in 1.0 M KOH electrolyte. (a) Electrocatalytic OER performances of FeNi-LDH/NF, A-S-FeNi/NF, RuO$_2$/NF and NF electrocatalysts with *iR* correction (85%), and (c) the corresponding Tafel plots. (b) Electrocatalytic HER performances of various electrocatalysts with *iR* correction (85%), and (d) the corresponding Tafel plots. (e) Polarization curves of two-electrode materials for overall water splitting without *iR* correction. (f) Stability test of A-S-FeNi/NF‖C-S-FeNi/NF by keeping the potential at 1.81 V (without *iR* compensation) for 200 h (with an initial current density of 100 mA cm^{-2}).

FeNi-LDH/NF (51.9 mV dec^{-1}) and RuO$_2$/NF (50.1 mV dec^{-1}). The electrochemical impedance spectra (EIS) and double-layer capacitances (C$_{dl}$) for FeNi-LDH/NF and A-S-FeNi/NF are shown in Fig. S11. As seen, the S-treatment can not only enhance charge transfer by reducing resistance (R$_{ct}$) [48], but also increase the number of active sites because C$_{dl}$ of A-S-FeNi/NF (58.3 mF cm^{-2}) is about 10 times larger than that of FeNi-LDH/NF (5.5 mF cm^{-2}) [49]. The OER performance of the A-S-FeNi-NF catalyst is compared with recently reported state-of-the-art earth-abundant OER catalysts in Table S3.

Of importance, the C-S-FeNi/NF catalyst also exhibits superior activity in alkaline HER (1.0 M KOH electrolyte, pH=13.8). In Fig. 4b, the commercial 20 wt% Pt/C offers the best catalytic activity with a low overpotential of 25 mV at a current density of 10 mA cm^{-2} [50,51]. Considering the non-noble metal composition, C-S-FeNi/NF shows a

satisfactory overpotential of 85.5 mV, which is much lower than that of FeNi-LDH/NF (150.5 mV @ 10 mA cm^{-2}) and other catalysts (Table S3). The Tafel slope of HER on C-S-FeNi/NF is 93.4 mV dec^{-1} (Fig. 4d), indicating a combined Volmer-Heyrovsky reaction path [51, 52]. The EIS spectra and C$_{dl}$ values of FeNi-LDH/NF and C-S-FeNi/NF in HER are also compared in Fig. S12. The Nyquist plots reveal that the charge transfer resistance of C-S-FeNi/NF (18.8 Ω) is much lower than that of FeNi-LDH/NF (30.5 Ω), implying a faster reaction rate at catalyst/electrolyte interfaces upon S-treatment. The Faradic efficiencies for producing O$_2$ and H$_2$ are also shown in Fig. S13, with the values more than 95% for both OER and HER.

Fig. S14 shows that the A-S-FeNi/NF catalyst exhibits outstanding durability. In Fig. S14b the polarization curve does not obviously change after 5000 cyclic voltammetry (CV) sweeps in alkaline OER. Moreover,

A-S-FeNi/NF can maintain current densities of 40 and 100 mA cm^{-2} (keeping the overpotentials at 246 and 263 mV, respectively) for more than 70 h without activity loss (Fig. S14a). The HER stability on C-S-FeNi/NF can be seen in Fig. S14c and d. In Fig. S14d the polarization curve is unchanged after 2000 cycles, and only slightly shifts after 5000 cycles. The high HER stability of C-S-FeNi/NF is also demonstrated by the current density versus time response as shown in Fig. S14c, in which the activity of FeNi-LDH/NF decrease by 50% within 3 h, while C-S-FeNi/NF can maintain the current density of 100 mA cm^{-2} for more than 20 h. The above results together prove that the S-FeNi/NF catalyst after several reaction cycles is stable in the alkaline environment for both OER and HER. The stability of such electronic structure and morphology in A-S-FeNi/NF and C-S-FeNi/NF are also demonstrated with XAS and TEM after long-time reactions (Figs. S15 and S16). *In-situ* XANES spectra of A-S-FeNi/NF at the Fe *K*-edge are shown in Fig. S17, which show no spectral changes in the whole OER process suggesting a stable structure.

The S-FeNi/NF catalyst after reaction restructuring is then evaluated as bi-functional catalyst at both anode (A-S-FeNi/NF) and cathode (C-S-FeNi/NF) for overall water splitting. As seen in Fig. 4e, the combination of A-S-FeNi/NF and C-S-FeNi/NF can deliver current densities of 10 and 100 mA cm^{-2} at cell voltages of 1.53 and 1.81 V, respectively, which are lower than those of state-of-the-art Pt/C-RuO$_2$/NF electrodes (1.55 and 1.90 V). Moreover, the combination of A-S-FeNi/NF and C-S-FeNi/NF can maintain the current density of 100 mA cm^{-2} (keeping the potential at 1.81 V) for more than 200 h without obvious decay as shown in Fig. 4f, suggesting excellent stability in overall water splitting. With the outstanding activity, a two-electrode electrolyzer using A-S-FeNi/NF and C-S-FeNi/NF catalysts as anode and cathode can thus be easily powered by an AA battery. Bubbles can be clearly observed in the system (Fig. S18).

3.4. Working mechanism

The working mechanism has been carefully studied. The catalytic performance has been significantly enhanced from FeNi-LDH/NF to S-FeNi/NF, suggesting the positive effect of S. The metal-S sites may act as the catalytic center to improve the performance. However, after OER reaction the metal-S signal disappears in the surface-sensitive XPS due to restructuring, suggesting that the surface metal-S components are not the active sites for long-term catalysis. On the contrary, from the bulk-sensitive XAS, especially at the S *K*-edge, the metal-S signal can be clearly observed even after 5000 cycles, strongly confirming the existence of metal-S sites in the sub-layer or bulk regions of the catalyst. Typically, the catalytic process mainly occurs at the solution/electrode interface with an easy contact between the surface catalytic sites and the reactants. The reaction can also occur at the sub-layer sites with the reactants crossing over the surface through defect parts. However, it will be much difficult for the reactants to transfer from the surface into the deeper bulk part with the block of many solid layers. Thus the sub-layer active sites of metal-S created after reaction restructuring should be responsible for the accelerated reaction, which can also be protected by the surface layer to maintain a long-term activity. It should be noted that the signal of SO$_4^{2-}$ can also be observed in the whole reaction process, which may partly come from the oxidized S in solution. As an effect of S-treatment, it might also contribute to the enhanced performance. To clarify this issue, we have immersed FeNi-LDH/NF in 0.5 M FeSO$_4$ solution with abundant SO$_4^{2-}$ for several minutes to create more SO$_4^{2-}$ sites on FeNi-LDH/NF, and show the corresponding OER performance in Fig. S19. Interestingly, the presence of SO$_4^{2-}$ shows no improvement to the OER performance of FeNi-LDH/NF, suggesting that the SO$_4^{2-}$ based sites are not the active sites for OER in this work (it might be active in other systems but contributes a little here). Thus the sub-layer metal-S components with good activity and high stability are the true active sites for the present efficient and stable alkaline water splitting.

Based on the experimental results, density functional theory (DFT)

calculations have been performed to obtain an in-depth understanding of the reaction mechanism. The A-S-FeNi/NF and C-S-FeNi/NF catalysts are modeled by adding a S dopant in the sub-layer of FeNi-LDH. In this configuration, the S dopant chemically bonds with Fe and Ni atoms. The top and side views of S-FeNi/NF are shown in Fig. S20. The catalytic activity of HER in alkaline media is significantly dependent on the reaction rate of water dissociation. As seen in Fig. 5a and b, the dissociation energy of the water molecule on C-S-FeNi/NF (-1.87 eV) is much more negative than that on FeNi-LDH/NF (-0.49 eV), indicating the water dissociation is thermodynamically preferred upon S-treatment for better HER.

The energy profiles of OER on FeNi-LDH have been extensively simulated, including our previous theoretical simulations [53,54]. The potential limiting step of OER is the conversion of *O to *OOH accompanied by a large overpotential [53]. After S-treatment, however, the OER proceeds along a new reaction path. As shown in Fig. 5c, the first step of OER is the addition of a hydroxyl group on the catalyst. DFT calculations show that the most stable binding site of OH is the sulfur atom. In the conditional OER mechanism, the second step is the conversion of *OH group to *O. On this surface, however, adding the second hydroxyl group on the Fe atom is the thermodynamically preferred reaction path. In the third step, the deprotonation of *O on the Fe atom occurs with a small energy increase of 0.68 eV. Subsequently, the formation of high energy *OOH can be achieved by a thermally activated combination of *O on Fe and *OH on S, which has an activation barrier of 1.326 eV. Please note that this step is not driven by electrochemistry and therefore does not cost electric energy. Similar cascaded thermo- and electro- catalytic water splitting have been reported recently, with different reaction paths [40,55]. Lastly, molecular oxygen is formed with small energy cost of less than 1.0 eV. Along this reaction path, there is no apparent theoretical overpotential as the energy penalty for *OOH production is shared by thermal and electrochemical processes. This new catalytic mechanism is quite general in the presence of suitable metal-S complexes in OER, and can therefore explain the enhanced catalytic activity in a number of S-treated metal oxides.

The working mechanism has been illustrated in Fig. 5d. S-based treatment can significantly enhance the catalytic performance of FeNi-LDH/NF for water splitting. In the reaction process, the catalyst will further change its structure and the final stable active sites have been revealed to be the metal-S sites buried in the sub-layer of the catalyst, which can show both high activity and good stability. The metal-S complexes can promote the water dissociation for better HER, while they can effectively accelerate the formation of high-energy peroxyl groups in anodes to achieve a high OER efficiency. Thus a highly efficient, stable, and low-cost bi-functional catalyst for both HER and OER can be obtained to achieve efficient overall water splitting. The working mechanism might be extended to various S-based treatments, and the creation of sub-layer active sites may guide the design for efficient and stable catalysts.

4. Conclusions

To summarize, S-FeNi/NF has been used as an excellent bi-functional catalyst for both anode and cathode, to achieve overall water splitting currents of 10 and 100 mA cm^{-2} at low cell voltages of 1.53 V and 1.81 V, respectively. The performance is better than the benchmark Pt/C-RuO$_2$ electrodes. The electronic structure of the catalysts at each reaction stages has been probed by XPS and XAS. The signal of metal sulfides such as Ni-S or Fe-S sites are clearly detected in S-FeNi/NF after the OER or HER reactions with the bulk-sensitive XAS, but not observed with the surface-sensitive XPS. The active metal-S sites responsible for the enhanced performance are actually located in the sub-layer of the catalyst. Theoretical calculations suggest S-Fe and S-Ni in the sub-layer can promote the water dissociation for better HER, and accelerate the formation of high-energy peroxyl groups for better OER, which are the origin of the high efficiency of electrolysis. The rational design with sub-
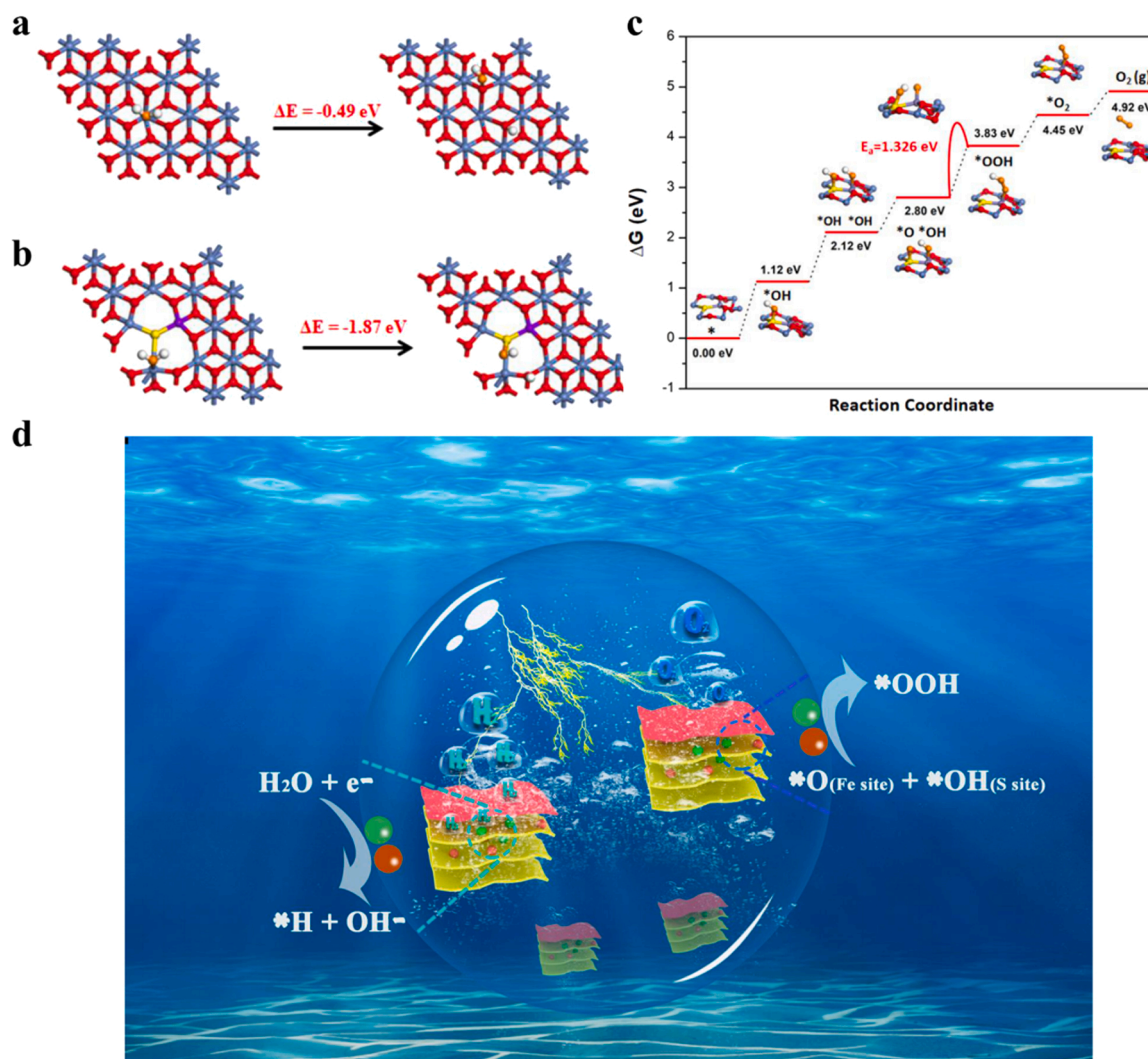
Fig. 5. Working mechanism. The atomic configurations and reaction energies of water dissociation on (a) FeNi-LDH and (b) S-doped FeNi-LDH. (c) The energy diagram of OER on A-S-FeNi/NF. The active site is S-Fe complex. The Ni, Fe, S, lattice O and O from solution are represented with light blue, purple, yellow, red and orange circles, respectively. (d) Illustration for the working mechanism on A-S-FeNi/NF and C-S-FeNi/NF.

layer active sites can both achieve a high efficiency and maintain a good stability, and thus should have fundamental and long-term impact on exploring new water splitting catalysts.

CRediT authorship contribution statement

Kun Feng: Data curation, Visualization. **Ruru Song:** Investigation. **Jiabin Xu:** Investigation. **Yufeng Chen:** Formal analysis. **Cheng Lu:** Formal analysis. **Youyong Li:** Software. **Werner Hofer:** Investigation. **Haiping Lin:** Software, Supervision. **Zhenhui Kang:** Conceptualization, Funding acquisition, Writing – review & editing, Supervision. **Jun Zhong:** Writing – review & editing, Supervision.

Declaration of Competing Interest

The authors declare that they have no known competing financial interests or personal relationships that could have appeared to influence the work reported in this paper.

Data availability

Data will be made available on request.

Appendix A. Supplementary material

Supplementary data associated with this article can be found in the online version at doi:10.1016/j.apcatb.2023.122365.

References

[1] B. Xiong, L. Chen, J. Shi, Anion-containing noble-metal-free bifunctional electrocatalysts for overall water splitting, ACS Catal. 8 (2018) 3688–3707.

[2] I. Roger, M.A. Shipman, M.D. Symes, Earth-abundant catalysts for electrochemical and photoelectrochemical water splitting, Nat. Rev. Chem. 1 (2017) 0003.

[3] S.S.A. Shah, T. Najam, M.K. Aslam, M. Ashfaq, M.M. Rahman, K. Wang, P. Tsiakaras, S. Song, Y. Wang, Recent advances on oxygen reduction electrocatalysis: correlating the characteristic properties of metal organic frameworks and the derived nanomaterials, Appl. Catal. B Environ. 268 (2020), 118570.

[4] Q. Shi, C. Zhu, D. Du, Y. Lin, Robust noble metal-based electrocatalysts for oxygen evolution reaction, Chem. Soc. Rev. 48 (2019) 3181–3192.

[5] Y. Gao, S. Qian, H. Wang, W. Yuan, Y. Fan, N. Cheng, H. Xue, T. Jiang, J. Tian, Boron-doping on the surface mediated low-valence Co centers in cobalt phosphide for improved electrocatalytic hydrogen evolution, Appl. Catal. B Environ. 320 (2023), 122014.

[6] C. Liu, Y. Han, L. Yao, L. Liang, J. He, Q. Hao, J. Zhang, Y. Li, H. Liu, Engineering bimetallic NiFe-based hydroxides/selenides heterostructure nanosheet arrays for highly-efficient oxygen evolution reaction, Small 17 (2021) 2007334.

[7] S. Wang, Y. Cao, W. Jia, Z. Lu, D. Jia, A cage-confinement strategy to fabricate Pt-Mo$_6$Co$_6$C heterojunction for highly efficient PH-universal hydrogen evolution, Appl. Catal. B Environ. 298 (2021), 120579.

[8] J. Lee, A. Kumar, T. Yang, X. Liu, A.R. Jadhav, G.H. Park, Y. Hwang, J. Yu, C.T. K. Nguyen, Y. Liu, S. Ajmal, M.G. Kim, H. Lee, Stabilizing the OOH* intermediate via pre-adsorbed surface oxygen of a single Ru atom-bimetallic alloy for ultralow overpotential oxygen generation, Energy Environ. Sci. 13 (2020) 5152–5164.

[9] F.S.M. Ali, R.L. Arevalo, M. Vandichel, F. Speck, E.-L. Rautama, H. Jiang, O. Sorsa, K. Mustonen, S. Cherevko, T. Kallio, Hydrogen evolution in alkaline medium on intratube and surface decorated PtRu catalyst, Appl. Catal. B Environ. 315 (2022), 121541.

[10] J. Zhu, L. Hu, P. Zhao, L.Y.S. Lee, K.-Y. Wong, Recent advances in electrocatalytic hydrogen evolution using nanoparticles, Chem. Rev. 120 (2020) 851–918.

[11] A. Li, L. Zhang, F. Wang, L. Zhang, L. Li, H. Chen, Z. Wei, Rational design of porous Ni-Co-Fe ternary metal phosphides nanobricks as bifunctional electrocatalysts for efficient overall water splitting, Appl. Catal. B Environ. 310 (2022), 121353.

[12] Y. Zhao, Y. Gao, Z. Chen, Z. Li, T. Ma, Z. Wu, L. Wang, Trifle Pt coupled with NiFe hydroxide synthesized via corrosion engineering to boost the cleavage of water molecule for alkaline water-splitting, Appl. Catal. B Environ. 297 (2021) 120395.

[13] Y. Yang, H. Yao, Z. Yu, S.M. Islam, H. He, M. Yuan, Y. Yue, K. Xu, W. Hao, G. Sun, H. Li, S. Ma, P. Zapol, M.G. Kanatzidis, Hierarchical nanoassembly of MoS2/Co9S8/Ni3S2/Ni as a highly efficient electrocatalyst for overall water splitting in a wide pH range, J. Am. Chem. Soc. 141 (2019) 10417–10430.

[14] P. Zhai, Y. Zhang, Y. Wu, J. Gao, B. Zhang, S. Cao, Y. Zhang, Z. Li, L. Sun, J. Hou, Engineering active sites on hierarchical transition bimetal oxides/sulfides heterostructure array enabling robust overall water splitting, Nat. Commun. 11 (2020) 5462.

[15] Y. Liu, J. Wu, K.P. Hackenberg, J. Zhang, Y.M. Wang, Y. Yang, K. Keyshar, J. Gu, T. Ogitsu, R. Vajtai, J. Lou, P.M. Ajayan, Brandon C. Wood, B.I. Yakobson, Self-optimizing, highly surface-active layered metal dichalcogenide catalysts for hydrogen evolution, Nat. Energy 2 (2017) 17127.

[16] X. Zheng, Y. Cao, Z. Wu, W. Ding, T. Xue, J. Wang, Z. Chen, X. Han, Y. Deng, W. Hu, Rational design and spontaneous sulfurization of NiCo-(oxy) hydroxysulfides nanosheets with modulated local electronic configuration for enhancing oxygen electrocatalysis, Adv. Energy Mater. 12 (2022) 2103275.

[17] H. Liu, J. Cheng, W. He, Y. Li, J. Mao, X. Zheng, C. Chen, C. Cui, Q. Hao, Interfacial electronic modulation of Ni3S2 nanosheet arrays decorated with Au nanoparticles boosts overall water splitting, Appl. Catal. B Environ. 304 (2022), 120935.

[18] C. Liu, D. Jia, Q. Hao, X. Zheng, Y. Li, C. Tang, H. Liu, J. Zhang, X. Zheng, P-Doped iron–nickel sulfide nanosheet arrays for highly efficient overall water splitting, ACS Appl. Mater. Interfaces 11 (2019) 27667–27676.

[19] X. Zhang, X. Cui, Y. Sun, K. Qi, Z. Jin, S. Wei, W. Li, L. Zhang, W. Zheng, Nanoporous sulfur-doped copper oxide (Cu2OxS1−x) for overall water splitting, ACS Appl. Mater. Interfaces 10 (2018) 745–752.

[20] X. Yu, Z.-Y. Yu, X.-L. Zhang, P. Li, B. Sun, X. Gao, K. Yan, H. Liu, Y. Duan, M.-R. Gao, G. Wang, S.-H. Yu, Highly disordered cobalt oxide nanostructure induced by sulfur incorporation for efficient overall water splitting, Nano Energy 71 (2020), 104652.

[21] M. Lee, H.-S. Oh, M.K. Cho, J.-P. Ahn, Y.J. Hwang, B.K. Min, Activation of a Ni electrocatalyst through spontaneous transformation of nickel sulfide to nickel hydroxide in an oxygen evolution reaction, Appl. Catal. B Environ. 233 (2018) 130–135.

[22] X. Zou, Y. Wu, Y. Liu, D. Liu, W. Li, L. Gu, H. Liu, P. Wang, L. Sun, Y. Zhang, In situ generation of bifunctional, efficient Fe-based catalysts from mackinawite iron sulfide for water splitting, Chem 4 (2018) 1139–1152.

[23] P. Cai, J. Huang, J. Chen, Z. Wen, Oxygen-containing amorphous cobalt sulfide porous nanocubes as high-activity electrocatalysts for the oxygen evolution reaction in an akaline/neutral medium, Angew. Chem. Int. Ed. 56 (2017) 4858–4861.

[24] D. Cao, D. Liu, S. Chen, O.A. Moses, X. Chen, W. Xu, C. Wu, L. Zheng, S. Chu, H. Jiang, C. Wang, B. Ge, X. Wu, J. Zhang, L. Song, Operando X-ray spectroscopy visualizing the chameleon-like structural reconstruction on an oxygen evolution electrocatalyst, Energy Environ. Sci. 14 (2021) 906–915.

[25] J. Lin, P. Wang, H. Wang, C. Li, X. Si, J. Qi, J. Cao, Z. Zhong, W. Fei, J. Feng, Defect-rich heterogeneous MoS2/NiS2 nanosheets electrocatalysts for efficient overall water splitting, Adv. Sci. 6 (2019) 1900246.

[26] Q. Qin, L. Chen, T. Wei, X. Liu, MoS2/NiS Yolk–Shell Microsphere-based electrodes for overall water splitting and asymmetric supercapacitor, Small 15 (2019) 1803639.

[27] G. Kresse, J. Furthmüller, Efficient iterative schemes for ab initio total-energy calculations using a plane-wave basis set, Phys. Rev. B 54 (1996) 11169–11186.

[28] G. Kresse, J. Furthmüller, Efficiency of ab-initio total energy calculations for metals and semiconductors using a plane-wave basis set, Comput. Mater. Sci. 6 (1996) 15–50.

[29] J.P. Perdew, K. Burke, M. Ernzerhof, Generalized gradient approximation made simple, Phys. Rev. Lett. 77 (1996) 3865–3868.

[30] Y. Sun, J. Wu, Z. Zhang, Q. Liao, S. Zhang, X. Wang, Y. Xie, K. Ma, Z. Kang, Y. Zhang, Phase reconfiguration of multivalent nickel sulfides in hydrogen evolution, Energy Environ. Sci. 15 (2022) 633–644.

[31] G. Zhang, Y.L. Y. Zhou, F. Yang, NiFe layered-double-hydroxide-derived NiO-NiFe2O4/reduced graphene oxide architectures for enhanced electrocatalysis of alkaline water splitting, ChemElectroChem 3 (2016) 1927–1936.

[32] H. Sun, W. Zhang, J.-G. Li, Z. Li, X. Ao, K.-H. Xue, K.K. Ostrikov, J. Tang, C. Wang, Rh-engineered ultrathin NiFe-LDH nanosheets enable highly-efficient overall water splitting and urea electrolysis, Appl. Catal. B Environ. 284 (2021), 119740.

[33] Z.W. Gao, J.Y. Liu, X.M. Chen, X.L. Zheng, J. Mao, H. Liu, T. Ma, L. Li, W.C. Wang, X.W. Du, Engineering NiO/NiFe LDH intersection to bypass scaling relationship for oxygen evolution reaction via dynamic tridimensional adsorption of intermediates, Adv. Mater. 31 (2019) 1804769.

[34] G. Chen, T. Wang, J. Zhang, P. Liu, H. Sun, X. Zhuang, M. Chen, X. Feng, Accelerated hydrogen evolution kinetics on NiFe-layered double hydroxide electrocatalysts by tailoring water dissociation active sites, Adv. Mater. 30 (2018) 1706279.

[35] D. Brion, Etude par spectroscopie de photoelectrons de la degradation superficielle de FeS2, CuFeS2, ZnS et PbS à l'air et dans l'eau, Appl. Surf. Sci. 5 (1980) 133–152.

[36] S. Piontek, C. Andronescu, A. Zaichenko, B. Konkena, K. junge Puring, B. Marler, H. Antoni, I. Sinev, M. Mulher, D. Mollenhauer, B. Roldan Cuenya, W. Schuhmann, U.-P. Apfel, Influence of the Fe:Ni ratio and reaction temperature on the efficiency of (FexNi1−x)9S8 electrocatalysts applied in the hydrogen evolution reaction, ACS Catal. 8 (2018) 987–996.

[37] L. An, Y. Li, M. Luo, J. Yin, Y.-Q. Zhao, C. Xu, F. Cheng, Y. Yang, P. Xi, S. Guo, Atomic-level coupled interfaces and lattice distortion on CuS/NiS2 nanocrystals boost oxygen catalysis for flexible Zn-Air batteries, Adv. Funct. Mater. 27 (2017) 1703779.

[38] J. Zhang, W. Xiao, P. Xi, S. Xi, Y. Du, D. Gao, J. Ding, Activating and optimizing activity of CoS2 for hydrogen evolution reaction through the synergic effect of N dopants and S vacancies, ACS Energy Lett. 2 (2017) 1022–1028.

[39] J. Kim, Y.J. Choe, S.H. Kim, K. Jeong, Enhancing the decomposition of refractory contaminants on SO42–functionalized iron oxide to accommodate surface SO4-generated via radical transfer from OH, Appl. Catal. B Environ. 252 (2019) 62–76.

[40] K. Feng, D. Zhang, F. Liu, H. Li, J. Xu, Y. Xia, Y. Li, H. Lin, S. Wang, M. Shao, Z. Kang, J. Zhong, Highly efficient oxygen evolution by a thermocatalytic process cascaded electrocatalysis over sulfur-treated Fe-based metal–organic-frameworks, Adv. Energy Mater. 10 (2020) 2000184.

[41] A. Matamoros-Veloza, O. Cespedes, B.R.G. Johnson, T.M. Stawski, U. Terranova, N. H. de Leeuw, L.G. Benning, A highly reactive precursor in the iron sulfide system, Nat. Commun. 9 (2018) 3125.

[42] Z. Tan, L. Sharma, R. Kakkar, T. Meng, Y. Jiang, M. Cao, Arousing the reactive Fe sites in pyrite (FeS2) via integration of electronic structure reconfiguration and in situ electrochemical topotactic transformation for highly efficient oxygen evolution reaction, Inorg. Chem. 58 (2019) 7615–7627.

[43] D.A. Tryk, S. Kim, Y. Hu, W. Xing, D.A. Scherson, M.R. Antonio, V.Z. Leger, G. E. Blomgren, Electrochemical insertion of lithium into pyrite from nonaqueous electrolytes at room temperature: an in situ Fe K-edge X-ray absorption fine structure study, J. Phys. Chem. 99 (1995) 3732–3735.

[44] K. Feng, J. Xu, Y. Chen, S. Li, Z. Kang, J. Zhong, Positively charged Pt-based nanoreactor for efficient and stable hydrogen evolution, Adv. Sci. 9 (2022) 2203199.

[45] J. Deng, Q. Zhang, X. Lv, D. Zhang, H. Xu, D. Ma, J. Zhong, Understanding photoelectrochemical water oxidation with X-ray absorption spectroscopy, ACS Energy Lett. 5 (2020) 975–993.

[46] K. Xia, F. Weesner, W. Bleam, P. Helmke, P. Bloom, U. Skyllberg, XANES studies of oxidation states of sulfur in aquatic and soil humic substances, Soil Sci. Soc. Am. J. 62 (1998) 1240–1246.

[47] C. Hu, L. Zhang, Z.J. Zhao, A. Li, X. Chang, J. Gong, Synergism of geometric construction and electronic regulation: 3D Se-(NiCo)Sx /(OH)x nanosheets for highly efficient overall water splitting, Adv. Mater. 30 (2018) 1705538.

[48] Z. Chen, R. Wu, Y. Liu, Y. Ha, Y. Guo, D. Sun, M. Liu, F. Fang, Ultrafine Co nanoparticles encapsulated in carbon-nanotubes-grafted graphene sheets as advanced electrocatalysts for the hydrogen evolution reaction, Adv. Mater. 30 (2018) 1802011.

[49] Y. Yang, L.N. Dang, M.J. Shearer, H.Y. Sheng, W.J. Li, J. Chen, P. Xiao, Y.H. Zhang, R.J. Hamers, S. Jin, Highly active trimetallic NiFeCr layered double hydroxide electrocatalysts for oxygen evolution reaction, Adv. Energy Mater. 8 (2018) 1703189.

[50] D. Liu, X. Li, S. Chen, H. Yan, C. Wang, C. Wu, Y.A. Haleem, S. Duan, J. Lu, B. Ge, P. M. Ajayan, Y. Luo, J. Jiang, L. Song, Atomically dispersed platinum supported on curved carbon supports for efficient electrocatalytic hydrogen evolution, Nat. Energy 4 (2019) 512–518.

[51] C. Lei, Y. Wang, Y. Hou, P. Liu, J. Yang, T. Zhang, X. Zhuang, M. Chen, B. Yang, L. Lei, C. Yuan, M. Qiu, X. Feng, Efficient alkaline hydrogen evolution on atomically dispersed Ni–Nx species anchored porous carbon with embedded Ni

nanoparticles by accelerating water dissociation kinetics, Energy Environ. Sci. 12 (2019) 149–156.

[52] Z. Xing, C. Han, D. Wang, Q. Li, X. Yang, Ultrafine Pt nanoparticle-decorated Co (OH)$_2$ nanosheet arrays with enhanced catalytic activity toward hydrogen evolution, ACS Catal. 7 (2017) 7131–7135.

[53] X. Liu, X. Fan, H. Huang, H. Lin, J. Gao, Electronic modulation of oxygen evolution on metal doped NiFe layered double hydroxides, J. Colloid Interface Sci. 587 (2021) 385–392.

[54] D. Yang, Z. Su, Y. Chen, K. Srinivas, J. Gao, W. Zhang, Z. Wang, H. Lin, Electronic modulation of hierarchical spongy nanosheets toward efficient and stable water electrolysis, Small 17 (2021) 2006881.

[55] B. Jiang, X. Fan, Q. Dang, F. Liao, Y. Li, H. Lin, Z. Kang, M. Shao, Functionalization of metal oxides with thiocyanate groups: a general strategy for boosting oxygen evolution reaction in neutral media, Nano Energy 76 (2020), 105079.